Numerical Methods and Advanced Simulation in Biomechanics and Biological Processes

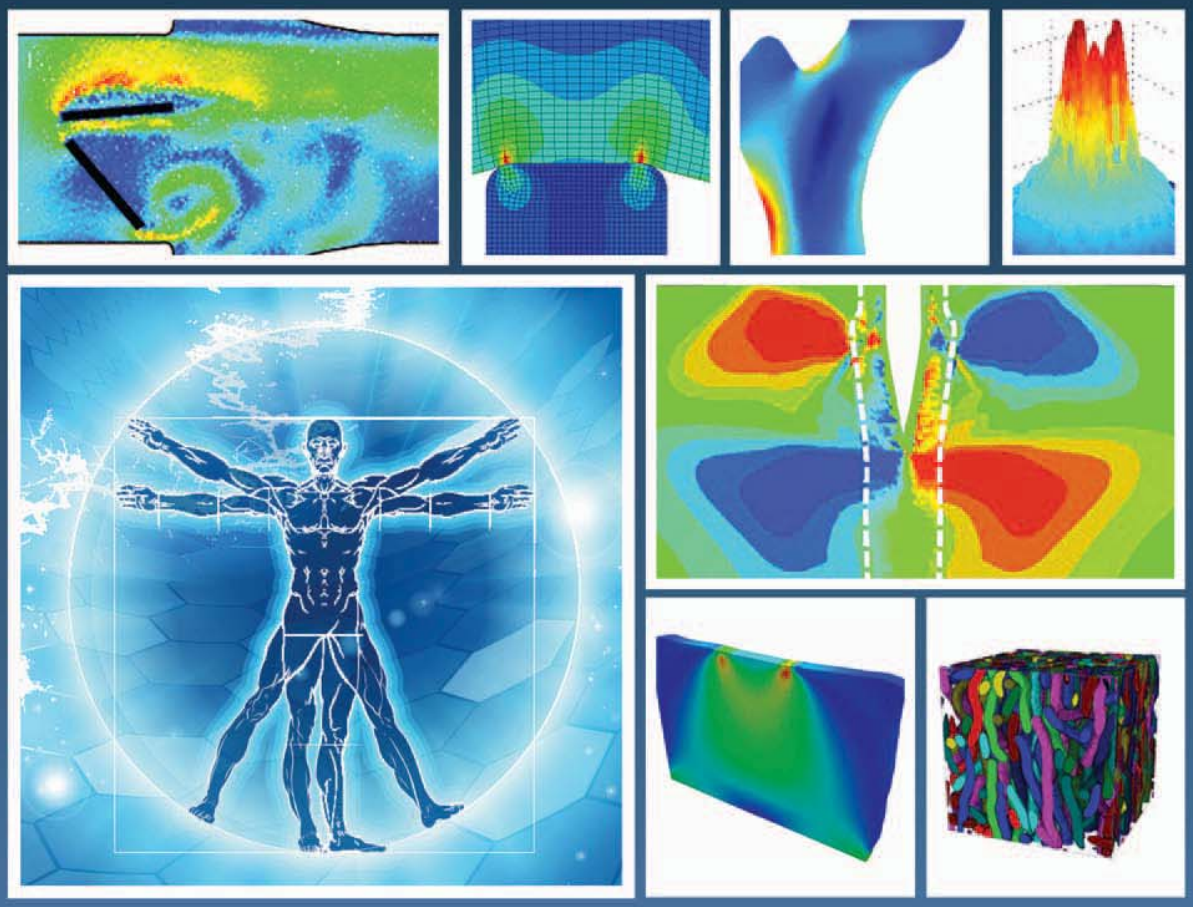

Edited by
Miguel Cerrolaza, Sandra J. Shefelbine
and Diego Garzón-Alvarado

Numerical Methods and Advanced Simulation in Biomechanics and Biological Processes

Edited by

Miguel Cerrolaza, Sandra J. Shefelbine
and Diego Garzón-Alvarado

ACADEMIC PRESS
An imprint of Elsevier

Academic Press is an imprint of Elsevier
125 London Wall, London EC2Y 5AS, United Kingdom
525 B Street, Suite 1800, San Diego, CA 92101-4495, United States
50 Hampshire Street, 5th Floor, Cambridge, MA 02139, United States
The Boulevard, Langford Lane, Kidlington, Oxford OX5 1GB, United Kingdom

Notices
Knowledge and best practice in this field are constantly changing. As new research and experience broaden our understanding, changes in research methods, professional practices, or medical treatment may become necessary.

Practitioners and researchers must always rely on their own experience and knowledge in evaluating and using any information, methods, compounds, or experiments described herein. In using such information or methods they should be mindful of their own safety and the safety of others, including parties for whom they have a professional responsibility.

To the fullest extent of the law, neither the Publisher nor the authors, contributors, or editors, assume any liability for any injury and/or damage to persons or property as a matter of products liability, negligence or otherwise, or from any use or operation of any methods, products, instructions, or ideas contained in the material herein.

Library of Congress Cataloging-in-Publication Data
A catalog record for this book is available from the Library of Congress

British Library Cataloguing-in-Publication Data
A catalogue record for this book is available from the British Library

ISBN: 978-0-12-811718-7

Publisher: Mara E. Conner
Acquisition Editor: Fiona Geraghty
Editorial Project Manager: Jennifer Pierce
Production Project Manager: Mohanapriyan Rajendran
Designer: Victoria Pearson

Typeset by TNQ Books and Journals

Chapter 20

Multicomponent Lattice Boltzmann Models for Biological Applications

A. Montessori[1], I. Halliday[2], M. Lauricella[3], S.V. Lishchuk[2], G. Pontrelli[3], T.J. Spencer[2] and S. Succi[3,4]
[1]*University of Rome "Roma Tre", Rome, Italy;* [2]*Sheffield Hallam University, United Kingdom;* [3]*Istituto per le Applicazioni del Calcolo - CNR, Roma, Italy;* [4]*Harvard University, Cambridge, MA, United States*

20.1 INTRODUCTION

In the last decade lattice Boltzmann (LB) methods have met with a huge success within the computational physics community because of their capability to simulate a very wide range of fluid dynamics phenomena and beyond. The LB models for fluid dynamics were first developed to cure some shortcomings of the lattice gas automata, such as the spurious invariants and the statistical noise, while preserving the local nature of the collisional and the linearity of the streaming operator along propagation characteristics. Since then, a great deal of effort has been devoted to the development of LB models capable of simulating complex flows across a wide range of scales of motion (Succi, 2015). In particular, LB models for nonideal fluids have seen a major boost in connection with the simulation of complex states of flowing matter, such as multiphase and multicomponent flows. The three basic LB multiphase methods are the color-fluid model (developed by Gunstensen et al., 1991.), the interparticle-potential model of Shan and Chen (1993), and the free-energy model (Swift et al., 1995). Here, we briefly outline the recent developments of each approach. The color-fluid model, proposed by Rothman and Keller (1988) and further developed by Grunau et al. (1993), is based on a two-component LB model, $f_{\alpha,i}(\mathbf{x}, t)$ and $f_{\beta,i}(\mathbf{x}, t)$, representing two different interacting fluids. The surface tension is encoded via a perturbation step namely, a modification of the original LB collision operator, while phase separation is maintained through a segregation step by forcing particles to regions of the same color. In the pseudopotential model (Shan and Chen, 1993) the interactions between fluid components are modeled through a modification of the collision operator by using an equilibrium velocity that includes an interactive force, which mimics an effective particle−particle potential at a mesoscopic level. This force guarantees phase separation and introduces surface tension effects. This model has been applied recently with considerable success (Montessori et al., 2015, Falcucci et al., 2013, Dollet et al., 2015). Moreover, it has been extended to include different van der Waals (vdW)−like equations of state by properly defining a suitable generalized functional form of the pseudopotential (Yuan and Schaefer, 2006, Qin, 2006). A multirange interaction model has been proposed to control the surface tension independently of the equation of state (Sbragaglia et al., 2007). The same can be done by modifying the attractive and repulsive terms of a vdW-like equation of state (Montessori et al., 2015). The free-energy model employs a free-energy function to include surface tension effects in a thermodynamically consistent manner (Orlandini et al., 1995). In addition to the methods outlined above, other promising methods based on a combination of the LB equation with explicit interface-tracking schemes are under development. One approach uses Peskin's (2002) distribution function for the interface force used in the immersed boundary (IB) method (Lallemand et al., 2007). More recently, interface tracking using the volume of fluid approach has been reported with promising results (Körner et al., 2005). In the following the pseudopotential approach for multiphase and multicomponent flows and the modified color-gradient method will be described in full detail, with a special emphasis on their prospective biological applications.

Numerical Methods and Advanced Simulation in Biomechanics and Biological Processes. https://doi.org/10.1016/B978-0-12-811718-7.00020-4

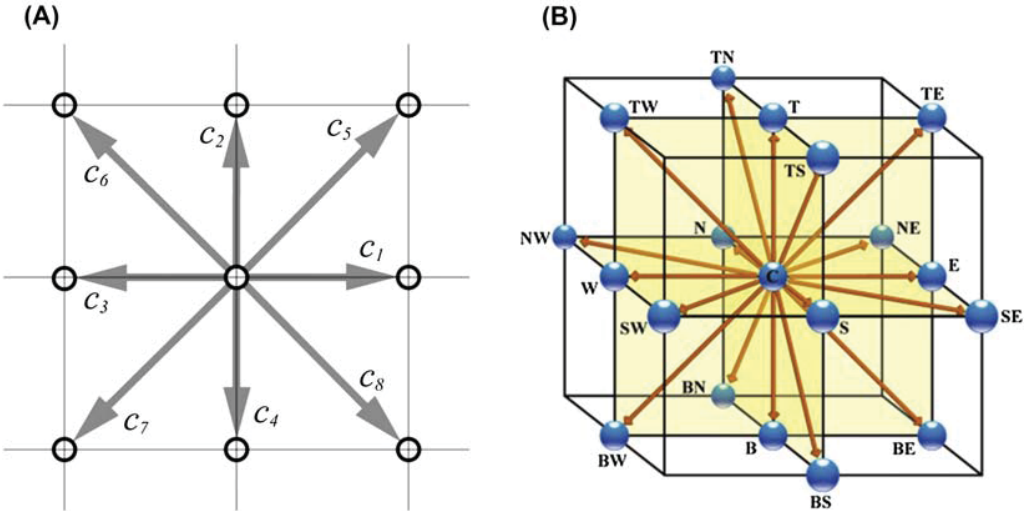

FIGURE 20.1 Sketch of the 9-speed two-dimensional (D2Q9) (A) and 19-speed three-dimensional lattices (D3Q19) (B).

20.2 THE LATTICE BOLTZMANN EQUATION

The LB equation with forcing terms reads as follows:

$$f_i(\mathbf{x}+\mathbf{c}_i\Delta t, t+\Delta t) - f_i(\mathbf{x},t) \;=\; -\omega\Delta t[f_i - f_i^{eq}(\rho, \mathbf{u}+\mathbf{F}/\omega\rho)] \tag{20.1}$$

where $f_i(\mathbf{x},\ t) \equiv f(\mathbf{x},\ \mathbf{v}=\mathbf{c}_i,\ t)$ is the discrete distribution function providing the probability of finding a particle at lattice site $\mathbf{x}$ at time t with discrete velocity $\mathbf{c}_i$, being i the lattice direction (Qian et al., 1992; Succi, 2001) (Fig. 20.1). In Eq. (20.1), ω is the relaxation parameter and $\mathbf{F}$ is a shift force.

Eq. (20.1) describes the evolution of the discrete single-particle distribution function in terms of *streaming* (left-hand side) and *collision*, in the form of a relaxation toward a local equilibrium (first term at right-hand side). The local equilibria are computed as second-order expansion in the local Mach number, $\mathrm{Ma} = u/c_s$, $\boldsymbol{u}$ being the macroscopic flow velocity and $c_s = \sqrt{1/3}$ the lattice speed of sound:

$$f_i^{eq}(\mathbf{x},t) \;=\; w_i\rho\left(1+\frac{\mathbf{u}\cdot\mathbf{c}_i}{c_s^2}+\frac{(\mathbf{u}\cdot\mathbf{c}_i)^2}{2c_s^4}-\frac{\mathbf{u}\cdot\mathbf{u}}{2c_s^2}\right) \tag{20.2}$$

where w_i are weights of the discrete equilibrium distribution functions and

$$\rho(\mathbf{x},t) \;=\; \sum_i f_i(\mathbf{x},t), \quad \mathbf{u}(\mathbf{x},t) \;=\; \frac{\sum_i f_i(\mathbf{x},t)\mathbf{c}_i}{\rho(\mathbf{x},t)} \tag{20.3}$$

the fluid density and the flow velocity, respectively. The second term at the right-hand side of Eq. (20.1) accounts for the effect of external/internal forces acting on the fluid molecules, such as gravity or, as we are going to describe in the following, a pseudomolecular interactive force that mimics an effective particle−particle potential at a mesoscopic level that promotes phase separation and introduces surface tension effects in a simple and efficient way (Shan and Chen, 1993).

20.3 THE PSEUDOPOTENTIAL APPROACH FOR MULTIPHASE AND MULTICOMPONENT FLOWS

In the Shan−Chen (SC) pseudopotential scheme, the nonideal force in Eq. (20.1) takes the form (Shan and Chen, 1993):

$$\mathbf{F}(\mathbf{x},t) \;=\; -G\psi(\rho(\mathbf{x},t))\Delta t\sum_i \lambda_i\mathbf{c}_i\psi(\rho(\mathbf{x}+\mathbf{c}_i\Delta t,t)) \tag{20.4}$$

where G is the strength of nonideal interactions, λ_i are the coefficients for the nth isotropic lattice, and the *generalized density* $\psi(\rho)$ contributes the excess pressure in the nonideal equation of state:

$$p = \rho c_s^2 + \frac{G}{2}\psi^2(\rho). \tag{20.5}$$

In the SC model, one has

$$\psi(\rho) = 1 - e^{-\rho} \tag{20.6}$$

which gives a critical pressure $p_c = (ln2 - 1/2)/3 \sim 0.063$ and a critical coupling $G_c = -4$. We recall that negative G's code for attraction, the only interaction in the SC model. Note that in the ideal gas limit $\rho \to 0$, the SC equation of state delivers $p = \rho c_s^2$, with a fixed sound speed $c_s^2 = 1/3$.

20.3.1 Discretization of the Nonideal Forcing Term on Higher-Order Lattices

Such spurious currents represent a serious tap to the numerical simulation of multiphase flows at substantial density ratios because their magnitude is directly related to the ratio between the densities of the coexisting phases. In pseudopotential multiphase models, spurious currents basically arise as a result of the lack of symmetry of the underlying lattice (Shan, 2006; Sbragaglia et al., 2007).

Improving the order of isotropy of the stencil employed to compute density gradient in SC-like models (see Fig. 20.2) may help in reducing the magnitude of such peripheral currents. Thus, a few additional comments on the implementation of pseudopotential forces on higher-order lattices are in order. By expanding the right-hand side of Eq. (20.4) in Taylor series, we obtain

$$\sum_i \lambda_i \psi(\mathbf{x} + \mathbf{c}_i \Delta t, t)\mathbf{c}_i = \nabla\psi \cdot E^{(2)} + \frac{1}{3!}\nabla^{(3)}\psi \cdot E^{(4)} + \frac{1}{5!}\nabla^{(5)}\psi \cdot E^{(6)} + \cdots \tag{20.7}$$

where the generic nth-order lattice tensor is defined as follows (Wolfram, 1986):

$$E^{(n)} = \sum_i \lambda_i c_{i\alpha_1} \cdots c_{i\alpha_n} \tag{20.8}$$

and the subscript α_j stands for the generic Cartesian component x, y, z. The quality of the left-hand side of Eq. (20.7) as an approximation of its continuum counterpart is strictly dictated by the degree of isotropy of the corresponding tensors $E^{(n)}$ (Shan, 2006). The main parameters of the higher-order lattices (Fig. 20.2) employed in (Montessori et al., 2015) are reported in Table 20.1.

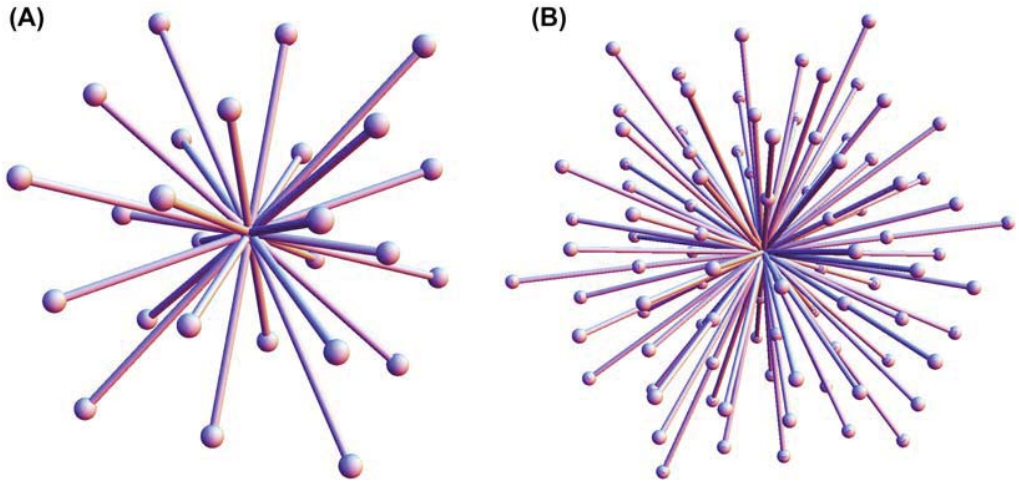

FIGURE 20.2 The set of discrete velocities for the fourth-order 27-speed (A) and of the eighth-order 93-speed lattices (B).

TABLE 20.1 Coefficients of the Isotropic $E^{(4)}$ (D3Q27F27) and $E^{(8)}$ (*D3Q27F93*) (See the Text for the Notation) Lattices in 3D Pseudopotential Models.

Energy Shell	$E^{(4)}$	$E^{(8)}$	Degeneracy
$\lambda(1)$	16/216	448/15120	6
$\lambda(2)$	4/216	240/15120	12
$\lambda(3)$	1/216	96/15120	8
$\lambda(4)$		50/15120	6
$\lambda(5)$		16/15120	24
$\lambda(6)$		8/15120	24
$\lambda(8)$		1/15120	12

The numbers in brackets refer to the energy $E = \sum_{j=x,y,z} c_{i\alpha_j}^2$ of the corresponding shell, the index i spanning the full set of discrete speeds. The degeneracy indicates the number of discrete speeds in the given energy shell

20.3.2 Nonideal Equations of State in Pseudopotentials Approach

The pseudopotential approach was recently improved to incorporate more realistic vdW equations of state. Montessori et al. (2015) developed a higher-order pseudopotential approach augmented with the Carnahan−Starling (CS) equation of state, which reads as follows (Carnahan and Starling, 1969):

$$p = \rho v_T^2 \frac{1+\gamma+\gamma^2-\gamma^3}{(1-\gamma)^3} - a\rho^2 \tag{20.9}$$

where $v_T = \sqrt{k_B T/m}$ is the thermal speed, $\gamma \equiv b\rho/4$, and a, b are the standard vdW parameters associated with the strength of long-range attraction and short-range repulsion. The fluid critical temperature and pressure, T_c and p_c, respectively, are controlled by a and b, according to the relation:

$$T_c = 0.3773a/b, \quad p_c = 0.0707a/b^2 \tag{20.10}$$

where the gas constant has been set to $R = 1$. Based on Eq. (20.5), the CS generalized density is computed as

$$\psi(\rho) = \sqrt{2\frac{p/c_s^2 - \rho}{G}}. \tag{20.11}$$

where G ensures the positivity of the term under the square root (Yuan and Schaefer, 2006). As compared to the standard vdW, the CS Eq. (20.9) is characterized by a steepening of the repulsive interactions in the hard-core region, which results in higher vapor/liquid density ratios at sufficiently high densities. We also note that the presence of a tunable thermal speed v_T in Eq. (20.9), instead of the fixed sound speed c_s in the SC equation of state. By lowering the absolute temperature T at a given value of the reduced temperature T/T_c, it is therefore possible to implement weaker gradients on the vapor phase, compared with the SC case. This feature is crucial for the stability of the vapor−liquid interface in the CS simulations (Colosqui et al., 2012).

20.3.3 Pseudopotential Approach for Interacting Multicomponent Fluids

We start from a kinetic LB equation for a multicomponent fluid with M species (Montessori et al., 2016) whose evolution equation is

$$f_{ni}(\mathbf{x}+c_i\Delta t, t+\Delta t) - f_{ni}(\mathbf{x},t) = -\omega_n \Delta t[f_{ni} - f_{ni}^{eq}(\rho_n, u + F_n/\omega_n\rho_n)] \tag{20.12}$$

where $f_{ni}(\mathbf{x}, t)$ (resp. ω_n) generalizes $f_i(\mathbf{x}, t)$ (resp. ω) for the species n=1, 2,…,M (cf., Eq. 20.1). To be noted that the equilibrium for the species n is a function of the local species density:

$$\rho_n(\mathbf{x},t) = \sum_i f_{ni}(\mathbf{x},t) \tag{20.13}$$

and the common, or barycentral, velocity is defined as

$$\mathbf{u}(\mathbf{x},t) = \frac{\sum_n \omega_n \sum_i f_{ni}(\mathbf{x},t)\mathbf{c}_i}{\sum_n \omega_n \rho_n(\mathbf{x},t)} \tag{20.14}$$

This common velocity receives a shift from the force $\mathbf{F}_n$ acting on the species n (Benzi et al., 2009). This force may be an external one or it could also be due to intermolecular potential interactions. In its first form the pseudopotential force within each species consisted of a purely repulsive action between the M species. Benzi et al. (2009) extended this formulation to model more complex states of fluid matter, such as foams and glassy states. In their work, they develop a model that is able to simulate a disjoining pressure, at a mesoscopic level, which can act as a foam stabilizer. To do so, the pseudopotential force within each species consists of an attractive (a) component acting only on the first Brillouin region (belt, for simplicity), and a repulsive (r) one acting on both belts, whereas the force between species (X) is short ranged and repulsive:

$$\mathbf{F}_n(\mathbf{x},t) = \mathbf{F}_n^a(\mathbf{x},t) + \mathbf{F}_n^r(\mathbf{x},t) + \mathbf{F}_n^X(\mathbf{x},t) \tag{20.15}$$

where

$$\mathbf{F}_n^a(\mathbf{x},t) = -G_n^a \psi_s(\mathbf{x},t) \sum_{i\in belt1} \lambda_i \psi_n(\mathbf{x}_i,t)\mathbf{c}_i \tag{20.16}$$

$$\mathbf{F}_n^r(\mathbf{x},t) = -G_n^r \psi_s(\mathbf{x},t) \sum_{i\in belt1\cup belt2} \lambda_i \psi_n(\mathbf{x}_i,t)\mathbf{c}_i \tag{20.17}$$

$$\mathbf{F}_n^X(\mathbf{x},t) = -\frac{\rho_s(\mathbf{x},t)}{\rho_{0n}^2} \sum_{s'\neq s} \sum_{i\in belt1} G_{nn'}\lambda_i \rho_{n'}(\mathbf{x}_i,t)\mathbf{c}_i \tag{20.18}$$

In the above, the sets $belt1$ and $belt2$ refer to the first and second Brillouin zones in the lattice (Benzi et al., 2009). Apart from a normalization factor, these correspond to the values given in (Sbragaglia et al., 2007). In addition, $G_{nn'} = G_{n'n}$, $n' = n$, is the cross-coupling between species, ρ_{0n} is a reference density, and, finally, $\mathbf{x}_i = \mathbf{x} + \mathbf{c}_i\Delta t$ are the displacements along the $\mathbf{c}_i$.

20.4 BIOFLUIDIC APPLICATIONS

The above methods have met with increasing popularity for the simulation of a broad variety of microfluidic flows, as we are going to detail in the sequel.

20.4.1 Droplet Dynamics With Applications to Biomicrofluidics

Recent advances in bio- and nanotechnologies have led to the development of novel microsystems for bioparticle separation and analysis. Microsystems are already revolutionizing the way we do science and have led to the development of a number of ultrasensitive bioanalytical devices capable of analyzing complex biological samples. These devices have application in a number of diverse areas, such as pollution monitoring, clinical diagnostics, drug discovery, and biohazard detection. A deeper understanding of the dynamics governing fluids at the microliter to picoliter scale is pivotal to gain a full knowledge of the physics governing such strikingly interesting phenomena and to help engineers in the design process. In this regard, computational fluid dynamics is a powerful tool, which can be effectively used to reduce the number of prototypes needed to develop a diagnostic device and provide deeper insight into the underlying mechanics of fluid systems. LB models, due to their inherent programming simplicity and scalability on multicore architectures, represent a hot bed for such applications. Recently, higher-order pseudopotential approaches augmented with vdW-like equations of state have been employed to simulate droplet off-axis collisions (Montessori et al., 2015), as reported in Fig. 20.3. In the fluid dynamic regime associated with the nondimensional parameters considered (see Montessori et al., 2015), the droplets are expected to (Qian and Law, 1997)

1. merge, as they get close to each other;
2. stretch and form a ligament, due to their initial momentum along opposite (parallel) directions;
3. break up the ligament, with a so-called end-pinching mechanism, due to their speed and momentum;
4. separate again, at a small deflection angle, due to the large impact parameter, with the formation of multiple satellite droplets.

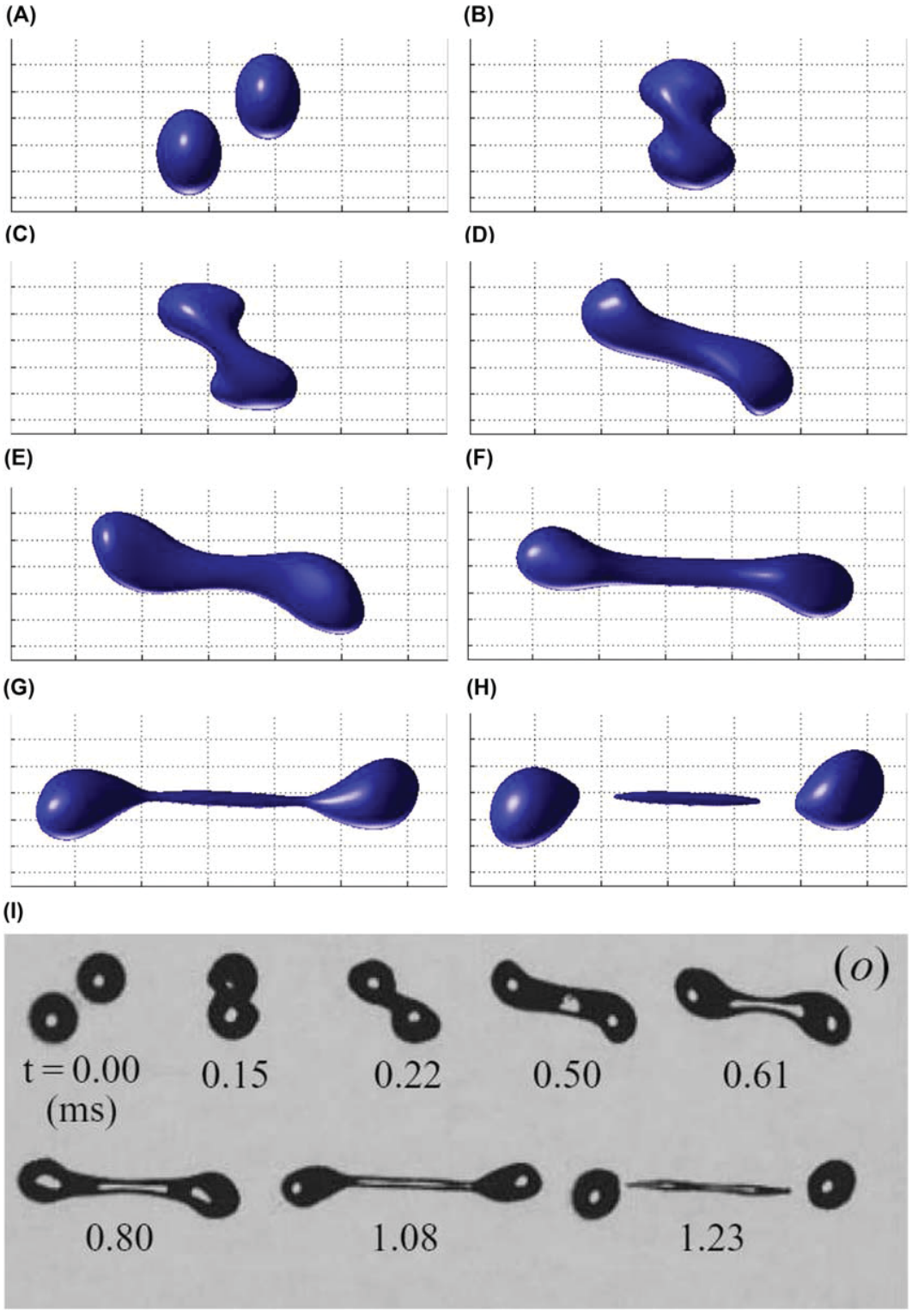

FIGURE 20.3 Off-axis collision between two droplets. The droplets are impulsively started with a horizontal speed $U/2 = \mp 0.09$ toward the opposite side of the computational domain. The Weber and Reynolds number of the simulation are We $\simeq$ 60.8 and Re $\simeq$ 313.7 and the density ratio is about 1:1000. The relaxation time is set to 0.62. The impact parameter is equal to 0.68 and the radius of the two droplets is set to 30 lattice points. The results are compared with those obtained by Qian and Law (1997). As one can see the evolution of the phenomenon is well captured by the numerical simulation. Indeed, as shown by the experiment, for this set of Reynolds and Weber, a kissinglike impact is performed after which a ligament appears that stretches and breaks up after an end-pinching mechanism. (A–H) Snapshots of the numerical simulation of the off-axis droplet impact. (I) Experimental results (Qian and Law, 1997). *Courtesy Montessori, A., Falcucci, G., La Rocca, M., Ansumali, S., Succi, S., 2015. Three-dimensional lattice pseudo-potentials for multiphase flow simulations at high density ratios. Journal of Statistical Physics 161 (6), 1404–1419.*

This is precisely the sequence of events emerging from the simulation, as reported in Fig. 20.3. It is to be noted that a water–air-like system is here considered, i.e., the density ratio between the light and heavy fluid is $\simeq 1000$. Notwithstanding the large density ratio, the density contours appear very neat, with no sign of numerical debris at any stage of this complex evolution, including the "critical" stages of merging and rupture. Moreover the evolution of the collision process is visually compared with the experiments carried out by Qian and Law. The results are in good agreement, at least qualitatively. Indeed the kissinglike merging process and the consequent ligament stretching followed by the end-pinching mechanism are well captured by the simulation.

Recently, Gupta and Sbragaglia (2014) investigated the effects of viscoelasticity on droplet dynamics and breakup in microfluidic in a T-junction geometry by means of a pseudopotentials multicomponent LB models coupled to a FENE-P (finitely extensible nonlinear elastic Peterlin) model (Gupta and Sbragaglia, 2014), employed to simulate the constitutive equations for finite extensible nonlinear elastic dumbbells.

It is worth noting that T-junction-like devices are currently employed in medical diagnostics, i.e., for chemical (enzymatic and nonenzymatic) reactions and cell analysis. In addition, droplet digital polymerase chain reaction represents a promising way to diagnose and manage cancer, avoiding expensive and invasive traditional biopsies and enabling frequent analysis of the tumor's molecular profile. Thus, the understanding of the fluid dynamics processes in these devices becomes fundamental for the designer to create and control tiny droplets with great precision, for example maintaining a consistent droplet size and frequency of droplet generation. Snapshot of the simulations for different values of the finite extensibility parameter of the FENE-P equation is reported in Fig. 20.4.

Kamali and Van den Akker (2013) also applied an SC-like approach to investigate the behavior of micron-sized droplets in complex geometries. Making use of the pseudopotential LB method, they simulated 2D dispersed gas–liquid flow through an inclined microchannel with two bends with applications in biological and biochemical processes. Dollet et al. (2015) employed a pseudopotential multicomponent approach with long-range repulsion for soft-glassy systems modeling to simulate the plastic rearrangement of emulsion in a quasi two-dimensional Hele-Shaw cell (Fig. 20.5). For the first time they highlighted a link between the localization lengthscale of the velocity profiles and that of plastic events across the channel, confirming the relevance of cooperativity for foams. These results confirm the capability of LB models to deal with extremely complex and physically rich fluid phenomena.

20.5 MODIFIED COLOR-GRADIENT METHOD

The dynamics of fluid–fluid boundaries are difficult to study because these interfaces are usually deformable and their shapes are not known a priori, being evolving in response to flow stresses.

Another classic method to model multicomponent fluids and multiphase flows in the continuum approximation dates back to Gunstensen et al. (1991). In it the phases are conveniently denoted by different colors, and interparticle interactions, responsible for phase separations, are modeled by a local color gradient, which is taken to give rise to an IB force (Peskin, 2002).

20.5.1 Two Immiscible Fluids

Let us consider two fluid distributions initially, which simultaneously occupy lattice link i, at position $\mathbf{x}$ and time t to be described by distribution functions, $f_{ri}(\mathbf{x}, t)$ and $f_{bi}(\mathbf{x}, t)$ (of course with $f_i(\mathbf{x},t) = f_{ri}(\mathbf{x}, t) + f_{bi}(\mathbf{x}, t)$). The nodal density of the red and blue fluid and their total density and momentum are defined as follows:

$$\rho_k = \sum_i f_{ki}, \ \rho_k \boldsymbol{u_k} = \sum_i \mathbf{c}_i f_{ki} \quad k = r, b$$

$$\rho = \rho_r + \rho_b, \ \rho \boldsymbol{u} = \rho_r \boldsymbol{u_r}, + \rho_b \boldsymbol{u_b}$$

In addition to the LB collision step, which operates on the distribution function f_i, there is an extra body-forcing or source term (which gives rise to a body force at the continuum scale) and a recoloring step in the model (Latva-Kokko and Rothman, 2005). In this step, the color at a node is redistributed to the kinetic-scale, postcollision distribution function $f_i^\dagger$ and then propagated as:

$$f_{ri}(\mathbf{x} + \mathbf{c}_i \Delta t, t + \Delta t) = \frac{\rho_r(\mathbf{x})}{\rho(\mathbf{x})} f_i^\dagger(\mathbf{x}, t) + \beta w_i \frac{\rho_r(\mathbf{x})\rho_b(\mathbf{x})}{\rho(\mathbf{x})} \mathbf{c}_i \cdot \widehat{\boldsymbol{n}}, \tag{20.19}$$

$$f_{bi}(\mathbf{x} + \mathbf{c}_i \Delta t, t + \Delta t) = \frac{\rho_b(\mathbf{x})}{\rho(\mathbf{x})} f_i^\dagger(\mathbf{x}, t) - \beta w_i \frac{\rho_r(\mathbf{x})\rho_b(\mathbf{x})}{\rho(\mathbf{x})} \mathbf{c}_i \cdot \widehat{\boldsymbol{n}}.$$

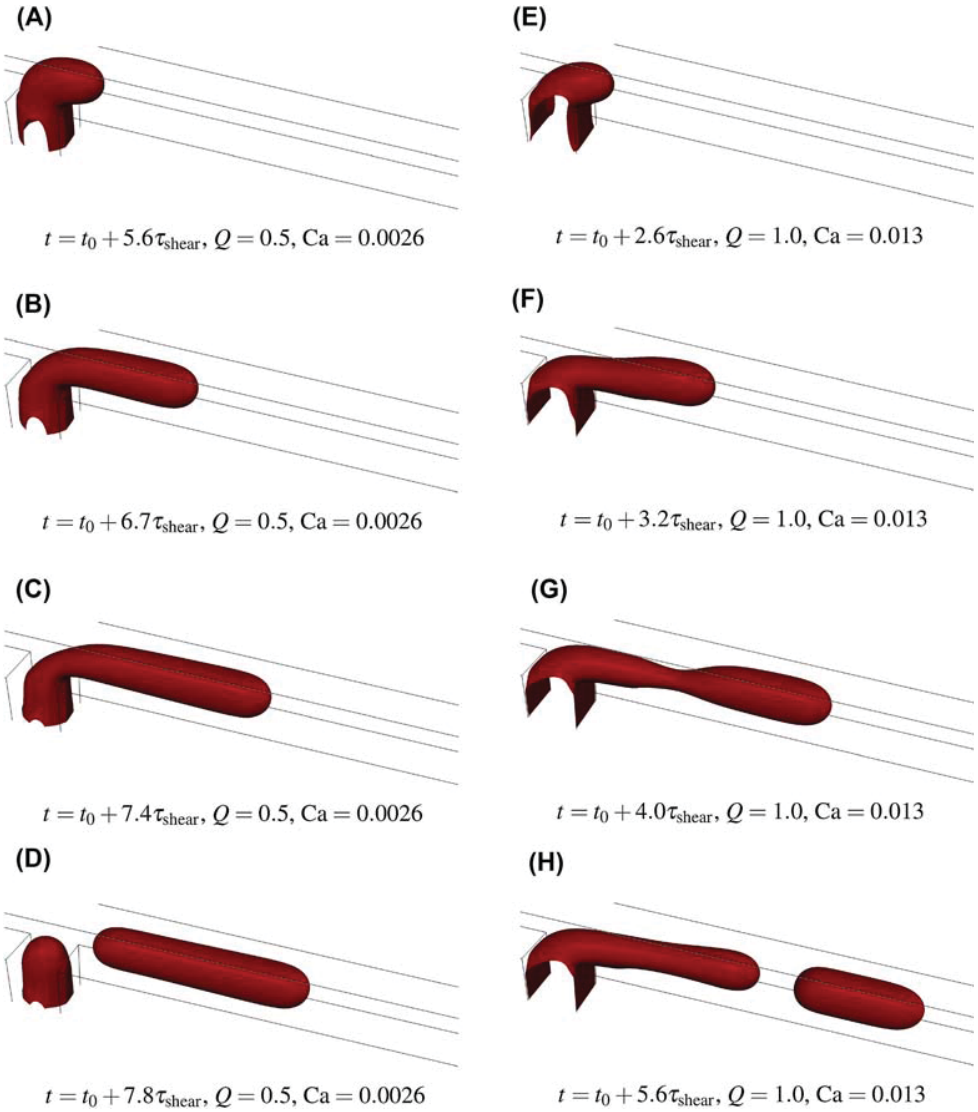

FIGURE 20.4 Droplet formation in T-junction geometries. Panels (A−D) illustrate the squeezing regime at Ca = 0.0026: the fluid thread enters and obstructs the main channel and breakup is mainly driven by the pressure buildup upstream of the emerging thread. Both the dynamics of breakup and the scaling of the sizes of droplets are influenced weakly by viscous forces. Panels (E−H) show typical features of the dripping regime at Ca = 0.013: the breakup process starts to be influenced by the shear forces, although the thread still occupies a significant portion of the main channel. This results in smaller droplets formed downstream of the T-junction. *Courtesy Gupta, A., Sbragaglia, M., 2016. A lattice Boltzmann study of the effects of viscoelasticity on droplet formation in microfluidic cross-junctions. The European Physical Journal E 39 (1), 1−15.*

Clearly, the above rule represents a balance between dispersion of color (first term) and its preferential redirection to a lattice region dominated by like color. The latter process is controlled by the segregation parameter β, discussed shortly. As a consequence of using the rule in Eq. (20.19), together with an appropriate IB force, a drop of red fluid will spontaneously form from an initially uniform mixture of red and blue fluid. In Eq. (20.19) the continuum scale interface normal $\hat{\boldsymbol{n}}$ is determined as follows. The local phase field is (Halliday et al., 2007)

$$\rho^N(\mathbf{x}, t) = \frac{\rho_r(\mathbf{x}, t) - \rho_b(\mathbf{x}, t)}{\rho_r(\mathbf{x}, t) + \rho_b(\mathbf{x}, t)}. \tag{20.20}$$

Surfaces of constant ρ^N value define the shape of the interfacial region with the surface $\rho^N = 0$ its center. Regions of the lattice characterized by $\rho^N = \pm 1$ are considered to contain pure, bulk fluids. Interfacial fluid occupies regions where $|\rho^N| < 1$.

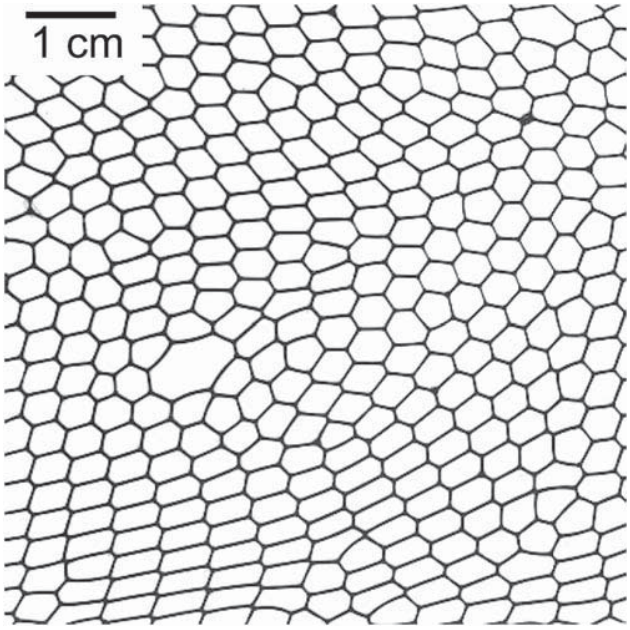

FIGURE 20.5 A snapshot of the bubbles in the foam flowing from left to right. *Courtesy Dollet, B., Scagliarini, A., Sbragaglia, M., 2015. Two-dimensional plastic flow of foams and emulsions in a channel: experiments and lattice Boltzmann simulations. Journal of Fluid Mechanics 766, 556–589.*

Throughout the narrow but distributed interfacial region, the local interface normal is determined using numerical gradients as

$$\widehat{\boldsymbol{n}} = -\frac{\nabla\rho^N}{|\nabla\rho^N|}. \tag{20.21}$$

For a red drop in a blue fluid, the interface normal unit vector, $\widehat{\boldsymbol{n}}$ points away from the enclosed red fluid. Local interfacial curvature is obtained from the surface gradient of $\widehat{\boldsymbol{n}} = (\widehat{n}_x, \widehat{n}_y)$, which, in 2D, is (Lishchuk et al., 2003)

$$\kappa \equiv \widehat{n}_x\widehat{n}_y\left(\frac{\partial\widehat{n}_y}{\partial x}+\frac{\partial\widehat{n}_x}{\partial y}\right)-\widehat{n}_y^2\frac{\partial\widehat{n}_x}{\partial x}-\widehat{n}_x^2\frac{\partial\widehat{n}_y}{\partial y}. \tag{20.22}$$

All the derivatives in Eqs. (20.21) and (20.22) may be computed to third-order accuracy if an appropriate stencil is used for the standard D2Q9 lattice (Halliday et al., 2013):

$$\frac{\partial f}{\partial x_\alpha} = \frac{1}{c_s^2}\sum_{i\neq 0} w_i f(\mathbf{x}+\boldsymbol{c}_i\Delta t)c_{i\alpha} + O\left(\boldsymbol{c}_i^4\right) \tag{20.23}$$

Eq. (20.19) can be analyzed and shown to generate a kinematically consistent interface profile (Halliday et al., 2007). For example, for a flat interface $\widehat{\boldsymbol{n}} = \widehat{\boldsymbol{e}}_x$ centered initially on x = 0, embedded within a fluid in uniform motion $\mathbf{u} = u_0\widehat{\boldsymbol{e}}_x$, one can show that the phase field is described by

$$\rho^N(\mathrm{x},t) = \tan h\,(\beta(\mathrm{x}-u_0t)), \tag{20.24}$$

which represents color kinematics appropriate to the continuum scale and immiscible components.

20.5.2 Many Mutually Immiscible Fluids

In fact, the segregation rule in Eq. (20.19) may be generalized straightforwardly to describe $M \gg 2$ mutually immiscible fluid components (Spencer et al., 2011) (see Section 20.3.3), each now identified by a subscript $n = 0,\ldots,M-1$ (with fluid $n = 0$ usually taken to be the background fluid):

$$f_{ni}(\mathbf{x}+\mathbf{c}_i\Delta t, t+\Delta t) = \frac{\rho_n(\mathbf{x})}{\rho(\mathbf{x})}f_i^{\dagger}(\mathbf{x},t) + w_i\sum_{m=0}^{M-1}\beta_{nm}\frac{\rho_n(\mathbf{x})\rho_m(\mathbf{x})}{\rho(\mathbf{x})}\,\mathbf{c}_i\cdot\widehat{\boldsymbol{n}}_{nm}, \tag{20.25}$$

where the colored densities are defined as follows:

$$\rho_n = \sum_i f_{ni}, \quad \rho = \sum_{n=0}^{M-1} \rho_n \tag{20.26}$$

and a set of phase fields and associated gradients define the interfacial normals:

$$\rho^N_{nm}(\mathbf{x},t) = \frac{\rho_n(\mathbf{x},t) - \rho_m(\mathbf{x},t)}{\rho_n(\mathbf{x},t) + \rho_m(\mathbf{x},t)}, \quad \widehat{\boldsymbol{n}}_{nm} = -\frac{\nabla\rho^N_{nm}}{\left|\nabla\rho^N_{nm}\right|}. \tag{20.27}$$

Note that it follows from the definition of the phase field that

$$\widehat{\boldsymbol{n}}_{nm} = -\widehat{\boldsymbol{n}}_{mn},$$

which means that color mass is conserved in Eq. (20.25). Now, if one makes additional assumptions regarding the absolute number of different fluids, which can be present at any lattice node, memory and execution speed scale only weakly with M, allowing for practical simulation of many, mutually immiscible drops or, indeed, vesicles (Dupin et al., 2004).

We defer further discussion of the application of this method to cellular-scale blood flow until we have accounted for the method by which the dynamics of a biological membrane may be encapsulated within multicomponent LB simulation.

20.6 MODELING MEMBRANES AS FLUID–FLUID INTERFACES

Correct interfacial kinematics arise from the segregation step previously considered: specifically, a kinematic property of mutual impenetrability emerges from the postcollision color segregation rules of the previous section. What we must now consider is the associated physical dynamics.

Generally, a spatially variable IB force distribution is applied to interfacial fluid (i.e., to regions of the lattice with $|\rho^N| < 1$) to recover target dynamic boundary conditions. A simple example is provided by the continuum scale force distribution $\mathbf{F} = \frac{1}{2}\sigma\kappa\nabla\rho^N$, which generates a Laplace pressure step of magnitude $\sigma\kappa$ between the separated bulk fluids (Lishchuk et al., 2003), along with a no-traction condition on tangential stress.

In this section, we consider a more complex class of interfaces such as closed membranes, which are defined as deformable boundaries separating two immiscible bulk fluids, each having conserved cross-sectional area. The enclosed liquid and membrane together form a vesicle. Unlike other interfacial problems where the area between the phases may increase or decrease, in the vesicle the total membrane or interface area is preserved, there being no mass exchange between the bilayer and the surrounding bulk fluid. However, like purely liquid–liquid boundaries, membranes can be regarded as an unsteady interface responsive to flow stresses between the segregated fluids.

On the foundation of the color-gradient model set out above, we have developed a Lishchuk-type force able to produce appropriate continuum scale membrane boundary conditions. Simulations that contain such a membrane achieve, e.g., a correct vesicle conformation by deforming and mediating appropriate physical stresses between the interior and exterior fluids. The detailed structure of a biological membrane's cytoskeleton and lipid bilayer is invisible at the continuum scale, so we adapt the approach of Kaoui et al. (2008) and postulate that interfacial fluid possesses properties representative of the membrane mechanics namely (1) preferred local curvature, (2) bending rigidity, (3) adjusted compressibility properties, (4) interfacial tension, and (5) conserved global length of the interfacial fluid. A representative force distribution derives from the variational derivative of an expression for overall membrane free energy incorporating effects (1)–(5) (Halliday et al., 2013). This force distribution is a normally directed, weighted fluid body force density acting only in the boundary region between the two fluids, i.e., on interfacial fluid:

$$\mathbf{F} = \frac{1}{2}\nabla\rho^N\left[\kappa\left(\sigma - \alpha\left(1 - \frac{l}{l_0}\right)\right) - \frac{b}{2}\kappa\left(\kappa^2 - \kappa_0^2\right) - b\frac{\partial^2\kappa}{\partial s^2}\right]. \tag{20.28}$$

In the above, s denotes distance measured along the direction of the membrane, $\frac{1}{2}\nabla\rho^N$ is a weight (Lishchuk et al., 2003), $\kappa(\kappa_0)$ the (preferred) interfacial curvature, α the interfacial compressibility, σ an interfacial tension further discussed below, $l(l_0)$ the (reference) length of the interface, and b its bending rigidity. Length l is maintained close to l_0 by allowing its value to modulate an effective interfacial tension $\sigma - \alpha\left(1 - \frac{l}{l_0}\right)$. That is, using that force density in Eq. (20.28), it results in an equilibrium shape, which is consistent with a constant enclosed volume, membrane cross-sectional area (length in 2D), membrane preferred curvature, and interfacial tension, which may nevertheless be deformed when external

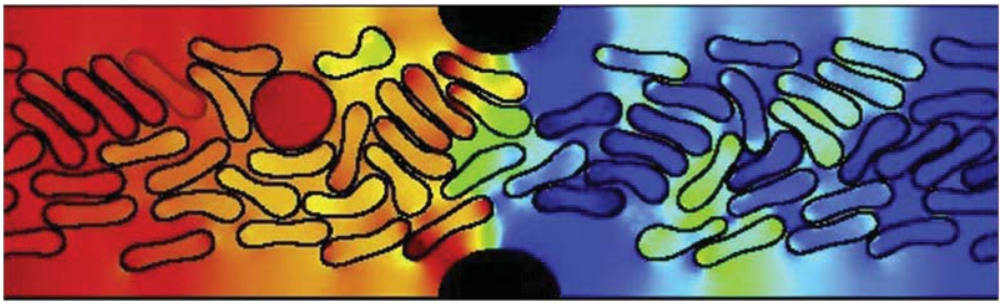

FIGURE 20.6 A snapshot of pressure driven flow of multiple vesicles in a channel with a constriction at $Re = 30$. Solid walls bound the domain, using the "link bounce-back method" (Succi, 2001). The pressure boundaries are implemented following Kim and Pitsch (2007). An exactly incompressible *D2Q9* lattice Bhatnagar–Gross–Krook model was used with vesicles' properties as follows, all expressed in lattice units: bending rigidity $b = 0.55$, surface tension $\sigma = 0.008$, membrane compressibility $\alpha = 0.15$, all fluids' segregation parameters $\beta_{nm} = 0.67$, $\forall n, m$, and the membrane preferred curvature $\kappa_0 = 0$. For the almost-circular (low deflation) vesicle preferred length $l_0 = 254$ and its initial lattice area was 5153. For the 58 deflated vesicles, preferred length was $l_0 = 224$ and their initial area was 2706. The velocity field has been initialized at rest, $\mathbf{u} = 0$ and the snapshot of the flow configuration was taken at time step $t = 4444800$. The overall simulation lattice is of size 999×297.

traction is applied, as the embedding fluid flows. Note that the constraint of constant vesicle volume is automatic as long as the enclosed fluid is incompressible and the parameterization of the membrane is direct. By selecting appropriate parameters, the deflation and deformability of vesicles may be readily adjusted (Halliday et al., 2013).

It is necessary briefly to consider how a spatially variable body force may be applied in LB simulation. The membrane force in Eq. (20.28) is applied as an external force density to what is effectively a single lattice fluid described by kinetic-scale distribution function $f_i = f_{ri} + f_{bi}$. Doolen et al. (1998) and Guo et al. (2002) generalized the lattice Bhatnagar–Gross–Krook model, originally devised by Qian et al. (1992), to describe lattice fluid subject to a known, spatially variable external force density, $\mathbf{F}$. Collision and forcing of the distribution function expressed in Eq. (20.1) may be straightforwardly reexpressed as

$$f_i^{\dagger} = f_i^{(0)}(\rho, \rho\mathbf{u}) + (1-\omega) f_i^{(1)}(\nabla\rho, \ldots \partial_x u_y \ldots, \mathbf{F}) + F_i(\omega, \mathbf{F}, \mathbf{u}), \tag{20.29}$$

where, recall, the dagger superscript indicates a postcollision, prepropagation quantity, and $f_i^{(0)}(\rho, \mathbf{u})$ denotes the equilibrium distribution function (Succi, 2001), and the source term, F_i, is

$$F_i = w_i\left(1 - \frac{\omega}{2}\right)\left(\frac{\mathbf{c}_i - \mathbf{u}}{c_s^2} + \frac{(\mathbf{c}_i \cdot \mathbf{u})(\mathbf{c}_i)}{c_s^4}\right) \cdot \mathbf{F}, \tag{20.30}$$

where all symbols have their usual meaning. Importantly, in the presence of an external force $\mathbf{F}$, the value of the fluid velocity depends on that external force (Guo et al., 2002):

$$\mathbf{u} = \frac{1}{\rho}\sum_i f_i \mathbf{c}_i + \frac{1}{2\rho}\mathbf{F}. \tag{20.31}$$

We return to this matter shortly. In the method outlined so far, all the dynamics and kinematics of the multifluid system of plasma and vesicle(s) is embedded within (1) force distribution and (2) the fluids' phase field. The method requires no set of constrained Lagrangian points to indicate the location of any of its potentially many interfaces (Halliday et al., 2013), and it inherits all the advantages of computational scaling with the number of immiscible components (i.e., vesicles) outlined in Section 20.5.2. Hence, little additional expense is incurred as the number of simulated vesicles increases beyond $N = 5$, to produce data such as that in Fig. 20.6. In the system represented there, there are >50 vesicles at representative concentration $c = 0.42$, with a range of deflations. A pressure gradient is applied to the system (regions of low (high) relative pressure are rendered blue (red)) and all the vesicles advect, deform, and order in response to the flow generated by the pressure gradient and the physics of their membranes. Simulation details may be found in the figure caption.

Although the data of Fig. 20.6 represent an efficient numerical solution to a very complex flow containing many interacting vesicles at high volume fraction, each vesicle shape evolves with the global membrane length (only) conserved. Implicitly, the constraint of global length conservation allows for different rates of strain in different membrane (interfacial fluid) regions, which in turn allows a variation of its tangential velocity. Such motion is only acceptable for a liquid drop. Put another way, the physical effect of uniform tangential motion (*tank-treading motion*) in the vesicle membrane is not recovered.

It was soon found that the method described so far must be enhanced if modalities associated with local incompressibility of membrane length elements are to be recovered from individual vesicles' fluid dynamics. We have recently introduced additional normal and tangential forces to encapsulate such effects. Enhanced dynamics is accomplished by adding to the body force density in expression (20.28) an additional contribution with a tangential component (Halliday et al., 2016):

$$\mathbf{F}' = \frac{1}{2}|\nabla\rho^N|\left(k\varepsilon\kappa\hat{\boldsymbol{n}} + k\frac{\partial\varepsilon}{\partial s}\hat{\boldsymbol{t}}\right), \tag{20.32}$$

where ε is a fictitious Hookean membrane strain and k its associated spring constant. The membrane strain field is computed from an explicit scheme solution of the equation:

$$\frac{\partial\varepsilon}{\partial t} = \frac{\partial u_t}{\partial s} - u_x\frac{\partial\varepsilon}{\partial x} - u_y\frac{\partial\varepsilon}{\partial y}, \tag{20.33}$$

where u_t is the local tangential velocity of the membrane. Upwinding is necessary to compute the derivatives in the right-hand side. Unfortunately, the solution ε of Eq. (20.33) is dependent on $\mathbf{u}$, which means that the correction force in Eq. (20.32) inherits a velocity dependence. Because $\mathbf{F}' = \mathbf{F}(\mathbf{u})$, Eqs. (20.31)–(20.33) must be solved by an iterative procedure (Halliday et al., 2016), to determine $\mathbf{u}$ and $\mathbf{F}'$.

Despite this elaborate procedure, the inclusion of $\mathbf{F}'$ introduces the tank-treading and tumbling behavior into the method, even for the quite deflated, biconcave shapes corresponding to red blood cells, at least in two dimensions, as we discuss this in the next section. In conclusion, notwithstanding the issue raised above, our approach dispenses entirely with the need explicitly to track the membrane, removes all need for computationally expensive and intricate interface tracking and remeshing, is completely Eulerian, and, not least, represents a two-way coupled vesicle membrane and flow within an LB framework.

20.7 FLUID-FILLED VESICLES IN A SHEAR FLOW

Vesicles are small structures consisting of an internal fluid enclosed by a lipid bilayer membrane, suspended in an external, aqueous solution. The physics of vesicles has attracted much theoretical and computational interest in recent decades. This is because of their ability to exhibit dynamical behaviors of relevance to living cells (such as red blood cells), the possibility of their exploitation as carriers of biomaterials (for example drugs), or their use in microencapsulation of active materials in drug delivery. Consequently, understanding the dynamical behavior of such deformable entities (shape, orientation, deformation, and migration), when the surrounding fluid is subject to shear, is an important issue worth investigating (Kaoui et al., 2009).

The physical properties of a vesicle membrane (surface tension, bending ratio, interfacial compressibility, etc.) originate at the molecular microscale, but, as we have shown above, they can be incorporated into a continuum-scale description by an effective hydrodynamic boundary condition based on an IB force distributions. In this section, the approach described previously is used to model one single suspended vesicle under shear flow, for a range of fluid viscosity contrasts (but no density contrast):

$$\Lambda = \frac{\eta_i}{\eta_e}$$

where η_i (η_e) is the shear viscosity of the internal (external) fluids and $\nu = \eta/\rho$ is the kinematic viscosity The data in Fig. 20.7 demonstrate our model's ability to recover a transition between tank-treading and tumbling. For a mild vesicle deflation 0.93, we denote the angular inclination with respect to the direction of undisturbed flow by θ (which is measured from the principal axes of the vesicle's inertia tensor). Where a steady inclination exists (identified in simulation $\frac{d\theta}{dt} \approx 0$) it is recorded. For $\Lambda > 2.5$ a steady inclination gives way to the unsteady, tumbling state. Again, refer to the figure caption for simulation data.

20.8 CONCLUSIONS

Summarizing, we have reviewed two major families of multicomponent LB models: pseudopotential methods and modified color-gradient methods. Both methods were originally intended to describe the dynamics of multicomponent and multiphase flows, such as droplets, foams, emulsions, and similar complex states of flowing matter. Lately, however, there has been a surge of interest in extending such models to the case of deformable bodies floating within a solvent fluid for problems of decided biological interest. The motivation is inherently computational, i.e., provide a fully Eulerian

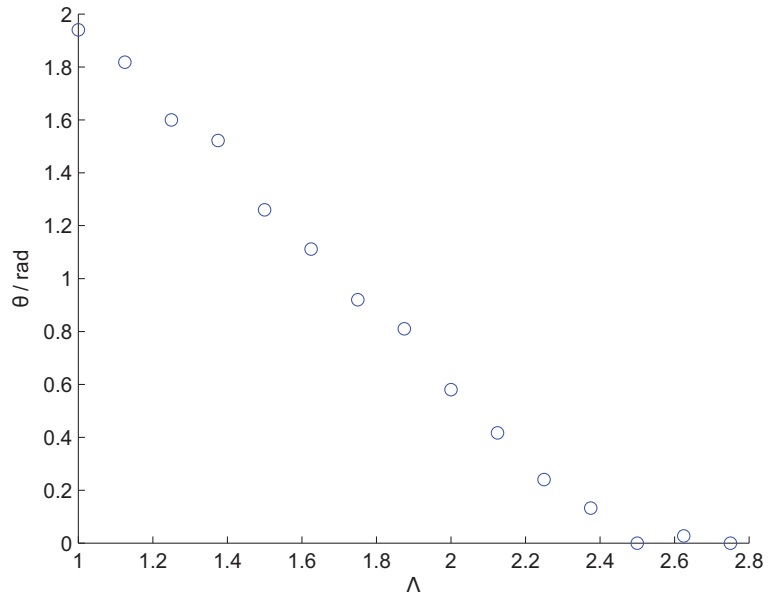

FIGURE 20.7 Data for a single vesicle with deflation 0.93 in a shear flow. The internal and external viscosities are in ratio Λ and the simulation was performed with lattice Bhatnagar–Gross–Krook with the external fluid parameterized by $\omega = 1$, $\nu = \frac{1}{6}$, $\beta = 0.67$. The angle θ denotes the steady inclination angle where it may be measured. For $\Lambda > 2.5$, $\theta \to 0$ tank-treading gives way to tumbling. The lattice dimensions were 131×105 lattice units.

alternative to mainstream Eulerian–Lagrangian techniques, whereby the fluid flow is typically solved by grid methods (including LB), whereas the motion of the deformable bodies is tracked by suitable off-grid particle methods. A realistic representation of the bodies may require a substantial amount of degrees of freedom, thereby considerably taxing the computational procedure, due to expensive interpolation/extrapolation procedures mapping the particles degrees of freedom to the grid and vice versa. In contrast, by letting the deformable interface dynamics emerge bottom-up from the specification of appropriate pseudopotentials and/or mesoscopic force fields incorporating the mechanical-elastic constraints, which characterized the body motion, the fully Eulerian approach would dispense from any fluid-particle coupling procedure. Albeit very appealing and potentially far reaching, the fully Eulerian approach still meets with a number of theoretical and computational challenges associated with the task of identifying the proper pseudopotentials and/or mesoscale forces and devises efficient procedures for their practical implementation on highly parallel computer platforms.

ACKNOWLEDGMENTS

This research has been funded from the European Research Council under the European Union's Seventh Framework Programme (FP/2007–2013)/ ERC Grant Agreement n. 306357 (ERC Starting Grant "NANO-JETS").

REFERENCES

Benzi, R., Sbragaglia, M., Succi, S., Bernaschi, M., Chibbaro, S., 2009. Mesoscopic lattice Boltzmann modeling of soft-glassy systems: theory and simulations. The Journal of Chemical Physics 131 (10), 104903.

Carnahan, N.F., Starling, K.E., 1969. Equation of state for nonattracting rigid spheres. The Journal of Chemical Physics 51 (2), 635–636.

Colosqui, C.E., Falcucci, G., Ubertini, S., Succi, S., 2012. Mesoscopic simulation of non-ideal fluids with self-tuning of the equation of state. Soft Matter 8 (14), 3798–3809.

Dollet, B., Scagliarini, A., Sbragaglia, M., 2015. Two-dimensional plastic flow of foams and emulsions in a channel: experiments and lattice Boltzmann simulations. Journal of Fluid Mechanics 766, 556–589.

Doolen, G.D., He, X., Chen, S., 1998. A novel thermal model for the lattice Boltzmann method in incompressible limit. Journal of Computational Physics 146, 282–300.

Dupin, M.M., Spencer, T.J., Halliday, I., Care, C.M., 2004. A many-component lattice Boltzmann equation simulation for transport of deformable particles. Philosophical Transactions of the Royal Society of London A: Mathematical, Physical and Engineering Sciences 362, 1885–1914.

Falcucci, G., Jannelli, E., Ubertini, S., Succi, S., 2013. Direct numerical evidence of stress-induced cavitation. Journal of Fluid Mechanics 728, 362–375.

Grunau, D., Chen, S., Eggert, K., 1989-1993. A lattice Boltzmann model for multiphase fluid flows. Physics of Fluids A: Fluid Dynamics 5 (10), 2557−2562.
Gunstensen, A.K., Rothman, D.H., Zaleski, S., Zanetti, G., 1991. Lattice Boltzmann model of immiscible fluids. Physical Review A 43 (8), 4320.
Guo, Z., Zheng, C., Shi, B., April 2002. Discrete lattice effects on the forcing term in the lattice Boltzmann method. Physical Review E 65, 046308.
Gupta, A., Sbragaglia, M., 2014. Deformation and breakup of viscoelastic droplets in confined shear flow. Physical Review E 90 (2), 023305.
Gupta, A., Sbragaglia, M., 2016. A lattice Boltzmann study of the effects of viscoelasticity on droplet formation in microfluidic cross-junctions. The European Physical Journal E 39 (1), 1−15.
Halliday, I., Hollis, A.P., Care, C.M., 2007. Lattice Boltzmann algorithm for continuum multicomponent flow. Physical Review E 76 (2), 026708.
Halliday, I., Lishchuk, S.V., Spencer, T.J., Pontrelli, G., Care, C.M., 2013. Multiple-component lattice Boltzmann equation for fluid-filled vesicles in flow. Physical Review E 87, 023307.
Halliday, I., Lishchuk, S.V., Spencer, T.J., Pontrelli, G., Evans, P.C., 2016. Local membrane length conservation in two-dimensional vesicle simulation using a multicomponent lattice Boltzmann equation method. Physical Review E 94, 023306.
Kamali, M.R., Van den Akker, H.E.A., 2013. Simulating gas-liquid flows by means of a pseudopotential lattice Boltzmann method. Industrial and Engineering Chemistry Research 52 (33), 11365−11377.
Kaoui, B., Ristow, G.H., Cantat, I., Misbah, C., Zimmermann, W., February 2008. Lateral migration of a two-dimensional vesicle in unbounded poiseuille flow. Physical Review E 77, 021903.
Kaoui, B., Biros, G., Misbah, C., October 2009. Why do red blood cells have asymmetric shapes even in a symmetric flow? Physical Review Letters 103, 188101.
Kim, S.H., Pitsch, H., 2007. A generalized periodic boundary condition for lattice Boltzmann method simulation of a pressure driven flow in a periodic geometry. Physics of Fluids 19 (10), 108101.
Körner, C., Thies, M., Hofmann, T., Thürey, N., Rüde, U., 2005. Lattice Boltzmann model for free surface flow for modeling foaming. Journal of Statistical Physics 121 (1−2), 179−196.
Lallemand, P., Luo, L.-S., Peng, Y., 2007. A lattice Boltzmann front-tracking method for interface dynamics with surface tension in two dimensions. Journal of Computational Physics 226 (2), 1367−1384.
Latva-Kokko, M., Rothman, D.H., 2005. Diffusion properties of gradient-based lattice Boltzmann models of immiscible fluids. Physical Review E 71 (5), 056702.
Lishchuk, S.V., Care, C.M., Halliday, I., 2003. Lattice Boltzmann algorithm for surface tension with greatly reduced microcurrents. Physical Review E 67, 036701.
Montessori, A., Falcucci, G., La Rocca, M., Ansumali, S., Succi, S., 2015. Three-dimensional lattice pseudo-potentials for multiphase flow simulations at high density ratios. Journal of Statistical Physics 161 (6), 1404−1419.
Montessori, A., Prestininzi, P., La Rocca, M., Falcucci, G., Succi, S., Kaxiras, E., 2016. Effects of Knudsen diffusivity on the effective reactivity of nanoporous catalyst media. Journal of Computational Science 17 (Part 2), 377−383.
Orlandini, E., Swift, M.R., Yeomans, J.M., 1995. A lattice Boltzmann model of binary-fluid mixtures. Europhysics Letters 32 (6), 463.
Peskin, C.S., 2002. The immersed boundary method. Acta Numerica 11, 479−517.
Qian, Y.H., d'Humieres, D., Lallemand, P., 1992. Lattice BGK models for Navier-Stokes equation. Europhysics Letters 17 (6), 479.
Qian, J., Law, C.K., 1997. Regimes of coalescence and separation in droplet collision. Journal of Fluid Mechanics 331, 59−80.
Qin, R.S., June 2006. Mesoscopic interparticle potentials in the lattice Boltzmann equation for multiphase fluids. Physical Review E 73, 066703. http://dx.doi.org/10.1103/PhysRevE.73.066703. URL: http://link.aps.org/doi/10.1103/PhysRevE.73.066703.
Rothman, D.H., Keller, J.M., 1988. Immiscible cellular-automaton fluids. Journal of Statistical Physics 52 (3−4), 1119−1127.
Swift, M.R., Osborn, W.R., Yeomans, J.M., 1995. Lattice Boltzmann simulation of nonideal fluids. Physical Review Letters 75 (5), 830.
Sbragaglia, M., Benzi, R., Biferale, L., Succi, S., Sugiyama, K., Toschi, F., 2007. Generalized lattice Boltzmann method with multirange pseudopotential. Physical Review E 75 (2), 026702.
Shan, X., 2006. Analysis and reduction of the spurious current in a class of multiphase lattice Boltzmann models. Physical Review E 73 (4), 047701.
Shan, X., Chen, H., 1993. Lattice Boltzmann model for simulating flows with multiple phases and components. Physical Review E 47 (3), 1815.
Spencer, T.J., Halliday, I., Care, C.M., 2011. A local lattice Boltzmann method for multiple immiscible fluids and dense suspensions of drops. Philosophical Transactions of the Royal Society of London A: Mathematical, Physical and Engineering Sciences 369 (1944), 2255−2263.
Succi, S., 2001. The Lattice Boltzmann Equation for Fluid Dynamics and Beyond. Oxford University Press.
Succi, S., 2015. Lattice Boltzmann 2038. Europhysics Letters 109 (5), 50001.
Wolfram, S., 1986. Cellular automaton fluids 1: basic theory. Journal of Statistical Physics 45 (3−4), 471−526.
Yuan, P., Schaefer, L., 2006. Equations of state in a lattice Boltzmann model. Physics of Fluids 18 (4), 042101.